

# Stimulated generation: extraction of energy from balanced flow by near-inertial waves

Cesar B. Rocha<sup>1†</sup>, Gregory L. Wagner<sup>2</sup> and William R. Young<sup>1</sup>

<sup>1</sup>Scripps Institution of Oceanography, University of California, San Diego

<sup>2</sup>Department of Earth, Atmospheric and Planetary Sciences, Massachusetts Institute of Technology

(Received xx; revised xx; accepted xx)

Primitive-equation numerical simulations and analysis of reduced models suggest that stimulated generation—the transfer of energy from balanced flows to existing internal waves—is a leading contender for an ocean mesoscale energy sink. Here we study stimulated generation using an asymptotic model that couples barotropic quasi-geostrophic flow and near-inertial waves with  $e^{imz}$  structure on the  $f$ -plane. A detailed description of the conservation laws of this vertical plane-wave model illuminates the mechanism of stimulated generation associated with vertical vorticity and lateral strain. In particular, there are two sources of wave potential energy, and corresponding sinks of balanced kinetic energy: (1) the refractive convergence of the wave action density into anti-cyclones (and divergence from cyclones) and (2) enhancement of wave-field gradients by geostrophic straining.

We quantify the energy conversion and describe the phenomenology of stimulated generation using numerical solutions of decaying ocean macroturbulence modified by near-inertial waves. The initial conditions are a uniform inertial oscillation and a two-dimensional turbulent field emergent from random initial conditions. In all solutions, stimulated generation co-exists with a transfer of balanced kinetic energy to large scales, which is associated with vortex merger. And geostrophic straining accounts for most of the generation of wave potential energy, which represents a sink of 10-20% of the initial balanced kinetic energy. But refraction is fundamental because it creates the initial eddy-scale lateral gradients in the near-inertial field that are then enhanced by advection. In these quasi-inviscid solutions, wave dispersion is the only mechanism that upsets stimulated generation: with barotropic balanced flow, lateral straining enhances the wave group velocity; the waves accelerate and thus rapidly escape from the straining regions. Because of this wave escape, the wave field does not suffer a direct cascade to dissipative scales.

**Key words:**

---

## 1. Introduction

The inverse cascade, acting on balanced ocean macroturbulence, transfers energy towards large spatial scales. But a statistically steady ocean circulation requires energy dissipation at the same rate as it is supplied by wind. Thus equilibration of the ocean

† Email address for correspondence: crocha@ucsd.edu

TABLE 1. Summary of model-based studies of energy extraction from balanced flow by near-inertial waves.

Study	Framework	<i>Stimulated generation</i> is referred to as
Gertz & Straub (2009)	Barotropic 2D double-gyre solutions coupled with forced 3D near-inertial waves.	<i>2D-to-3D energy transfer</i>
Thomas (2012)	Near-inertial waves in a baroclinic geostrophic flow undergoing frontogenesis.	<i>deformation shear production</i>
Taylor & Straub (2016)	Boussinesq channel-flow with both high- and low-frequency forcing.	<i>advective sink</i>
Barkan <i>et al.</i> (2016)	Boussinesq channel-flow with both high- and low-frequency forcing.	<i>direct extraction</i>
Shakespeare & Hogg (2017)	Boussinesq channel-flow with low-frequency forcing. Spontaneous generation in the surface layer and stimulated generation in the interior.	<i>interior amplification</i>

macroturbulence requires ageostrophic processes, acting in opposition to the inverse cascade, to produce a transfer of energy towards the centimeter scales at which molecular viscosity is effective. Mechanisms that might result in this down-scale transfer include, but are not limited to, surface and benthic boundary-layer turbulence, lee-wave generation by mesoscale eddies negotiating bottom topography, and the spontaneous generation of internal waves by upper-ocean frontal instabilities; see Nagai *et al.* (2015) for a recent review.

Here we focus on a mechanism first identified by Gertz & Straub (2009): externally-forced near-inertial waves might provide an energy sink for large-scale balanced flow. Since Gertz & Straub (2009), several other studies, summarized in table 1, have argued for significant energy transfer from balanced flows to near-inertial waves. A common aspect of the studies in table 1 is that the near-inertial waves are first introduced by forcing at the inertial frequency and then grow by extracting energy from the balanced flow.

To distinguish this mechanism from *spontaneous* generation, and to complete an electromagnetic analogy, Xie & Vanneste (2015) (XV hereafter) refer to the transfer of energy from balanced flow to externally forced near-inertial waves as *stimulated generation*. The more widely studied process of spontaneous generation is the emission of internal waves arising from the slow evolution of balanced flow in the absence of external forcing at wave frequencies (Vanneste 2013). Spontaneous generation is inefficient at small and moderate Rossby numbers and its global impact on the energetics of the ocean macroturbulence is probably small (Danioux *et al.* 2012; Nagai *et al.* 2015). Spontaneous generation is localized at sharp submeoscale fronts with order-one Rossby number (e.g., Shakespeare & Hogg 2017) while the stimulated variety operates even at small Rossby

numbers characteristic of most interior oceanic conditions, provided only that internal waves are introduced by external forcing. Throughout the ocean, internal waves are reliably forced by wind and tides and thus stimulated generation is a leading contender as a mesoscale energy sink. Alternative terms to stimulated generation used in the literature are summarized in table 1. The diversity of studies in table 1 indicates that stimulated generation is a common, and therefore probably important, wave mean flow interaction.

Using a variational formulation of the generalized Lagrangian mean, XV derived a phase-averaged model of the coupling between near-inertial waves and quasi-geostrophic (QG) flow. Wagner & Young (2016) derived a similar coupled model via Eulerian multiple-time expansion; these authors include the second harmonic of the primary near-inertial wave and simplify the wave dynamics by assuming moderate QG vertical shears. In both coupled models the near-inertial waves are governed by the equation of Young & Ben Jelloul (1997) (YBJ hereafter) and the balanced flow satisfies QG dynamics—the waves contribute phase-averaged quadratic terms to the QG potential vorticity (PV). Salmon (2016) provides a useful perspective on these “NIW-QG” models; without assuming that the waves are near-inertial, and within a single variational framework, Salmon unifies XV’s model with the wave-mean flow models of Bühler & McIntyre (1998) and Wagner & Young (2015).

A central feature of the NIW-QG model is that there are two integral energy conservation laws for (1) near-inertial kinetic energy and (2) the sum of near-inertial potential energy and total balanced energy. The NIW-QG model shows that stimulated generation is a consequence of the reduction in near-inertial wave length scales resulting from advection and refraction of waves by the balanced flow. Reduction of wave length scales is accompanied by an increase in wave potential energy, and because of conservation law (2), a reduction in the energy of the balanced flow.

Here we investigate perhaps the simplest example of stimulated generation obtained from the NIW-QG model by assuming barotropic QG flow and vertically-planar near-inertial waves. Because the balanced flow is barotropic, while the near-inertial wave is three dimensional, this “vertical plane-wave model” resembles the original scenario of Gertz & Straub (2009). We show that the convergence of wave kinetic energy into anti-cyclones and geostrophic straining of the waves reduces the wave length scale, amplifies gradients of wave amplitude, and converts balanced kinetic energy into near-inertial potential energy.

## 2. The vertical plane-wave model

The vertical plane wave model is obtained by assuming barotropic balanced flow, with streamfunction  $\psi(x, y, t)$ , a uniform background buoyancy frequency  $N_0$ , and a single vertically propagating wave with vertical structure  $e^{imz}$  and back-rotated wave velocity  $\phi(x, y, t)$ . With these idealizations, appendix A derives the vertical plane-wave model starting from the phase-averaged equations of Wagner & Young (2016); XV obtain the same model from their version of the phase-averaged equations. In either case, the leading-order velocity  $(u, v, w)$ , pressure  $p$ , and buoyancy  $b$  are:

$$u + iv = e^{i\varpi} \phi - \psi_y + i\psi_x; \quad (2.1)$$

$$w = im^{-1} e^{i\varpi} \partial \phi + cc; \quad (2.2)$$

$$p = -i\eta e^{i\varpi} \partial \phi + cc + f_0 \psi; \quad (2.3)$$

$$b = m\eta e^{i\varpi} \partial \phi + cc. \quad (2.4)$$

Above,  $\varpi = mz - f_0 t$  is the phase of the vertical plane wave,  $\eta = f_0 \lambda^2$  is the wave “dispersivity,” where  $\lambda = N_0 / f_0 m$  is a horizontal scale, cc denotes complex conjugate, and

$$\partial \stackrel{\text{def}}{=} \frac{1}{2}(\partial_x - i\partial_y) \quad (2.5)$$

is a differential operator. The complex field  $\phi(x, y, t)$  in (2.1) is the back-rotated velocity of the near-inertial waves; in (2.2)–(2.4) the other wave fields are expressed in terms of  $\partial\phi$ . The compact representation of the wave variables in terms of  $\phi$  follows YBJ; the balanced variables are represented by the familiar QG streamfunction  $\psi$ .

The PV of the balanced flow is expressed in terms of  $\psi$  and  $\phi$  by

$$q = \underbrace{\Delta\psi}_{\stackrel{\text{def}}{=} \zeta} + \underbrace{\frac{1}{f_0} \left[ \frac{1}{4} \Delta|\phi|^2 + \frac{i}{2} J(\phi^*, \phi) \right]}_{\stackrel{\text{def}}{=} q^w}, \quad (2.6)$$

where  $\Delta \stackrel{\text{def}}{=} \partial_x^2 + \partial_y^2$  is the horizontal Laplacian and  $J(f, g) \stackrel{\text{def}}{=} f_x g_y - f_y g_x$  is the Jacobian, and the superscript star  $*$  denotes complex conjugation. Equation (2.6) is the “inversion relation”:  $q$  and  $\phi$  determine the flow as  $\psi = \Delta^{-1}(q - q^w)$  where  $q^w$  defined in (2.6) is the “wave potential vorticity.” Once  $\psi$  is obtained by inversion, the field equations (2.7) and (2.8) below can be time-stepped.

Using the generalized Lagrangian mean formulation Böhler & McIntyre (1998) showed that the assumption of weak interaction between internal waves and balanced flow results in wave-averaged terms contributing to the materially conserved QGPV. In (2.6) this wave-averaged feedback on the balanced flow is expressed concisely in terms of the wave PV  $q^w$ .

The balanced flow evolves according to QGPV advection

$$q_t + J(\psi, q) = D_q; \quad (2.7)$$

the back-rotated velocity satisfies the wave equation

$$\phi_t + J(\psi, \phi) + \phi \frac{i}{2} \zeta - \frac{i}{2} \eta \Delta \phi = D_\phi. \quad (2.8)$$

$D_q$  and  $D_\phi$  in (2.7) and (2.8) are dissipative terms described below.

The wave equation (2.8) is the YBJ model in the case where the near-inertial wave has  $e^{imz}$  structure. The back-rotated wave velocity,  $\phi$ , evolves through dispersion—the last term on the left of (2.8)—and nonlinear advection and refraction by the second and third terms in (2.8). Without advection, (2.8) is analogous to Schrödinger’s equation (e.g., Landau & Lifshitz 2013, page 51). The relative vorticity,  $\Delta\psi$ , is the potential, with negative  $\Delta\psi$  a well, and the “dispersivity,”  $\frac{1}{2} f_0 \lambda^2$ , is Planck’s constant (Balmforth *et al.* 1998; Balmforth & Young 1999; Danioux *et al.* 2015). The quantum analogy may be useful for some readers, but it is not necessary for the understanding of the results below.

The terms on the right of (2.7) and (2.8),  $D_q$  and  $D_\phi$ , represent small-scale dissipation. Small-scale dissipation is necessary to absorb the forward transfers of potential enstrophy and wave kinetic and potential energies in the numerical solutions reported below. We find that biharmonic diffusion and viscosity,

$$D_q = -\kappa_e \Delta^2 q \quad \text{and} \quad D_\phi = -\nu_\phi \Delta^2 \phi, \quad (2.9)$$

are sufficient to extend the spectral resolution compared to Laplacian dissipation. In practice, we choose  $\kappa_e$  and  $\nu_\phi$  so that the highest 35% of the modes lie in the dissipation range and aliased wavenumbers are strongly damped.

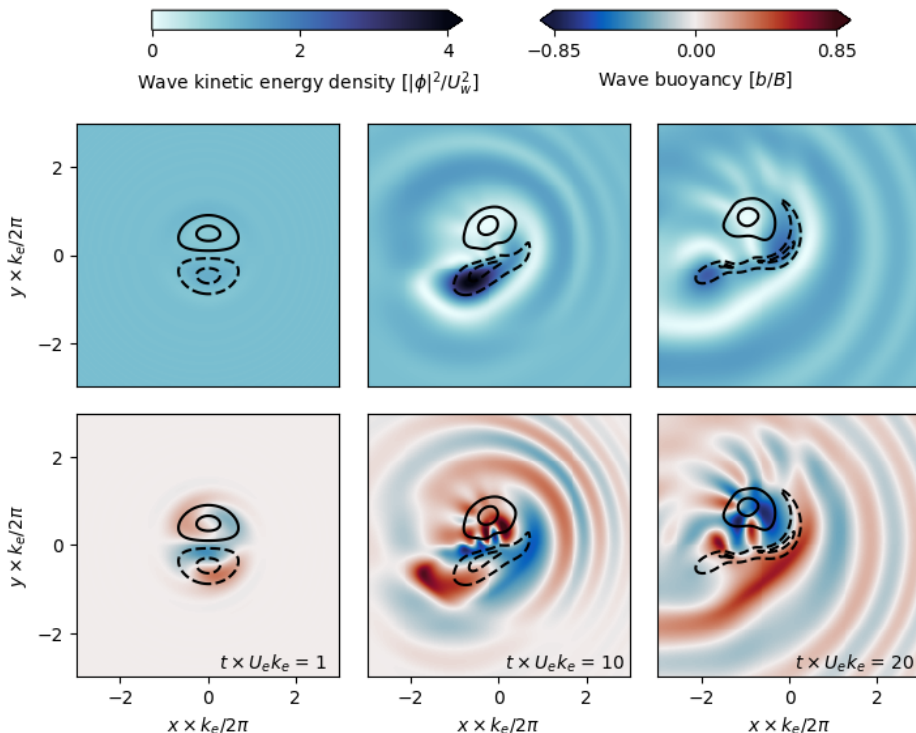


FIGURE 1. Snapshots of the Lamb-Chaplygin dipole solution with parameters presented in table 2. Contours depict potential vorticity,  $q/(U_e k_e) = [-1.5, -0.5, 0.5, 1.5]$ , with dashed lines showing negative values. The upper row shows the wave action density  $|\phi|^2/2f_0$ . The lower row shows the wave buoyancy; the buoyancy scale is  $B = k_e m U_w f_0 \lambda^2$ . These plots only show the central  $(1/5)^2$  of the simulation domain.

### 2.1. An illustrative solution: the Lamb-Chaplygin dipole

As a preamble to our discussion of stimulated generation in freely-evolving turbulence, we consider an example in which the initial QG flow is the Lamb-Chaplygin dipole—see figure 1. This dipole is an exact solution of the Euler equations on an infinite two-dimensional plane where the vorticity is confined to a circle of radius  $R$  (Meleshko & Van Heijst 1994). The relative vorticity, steady in a frame moving at uniform zonal velocity  $U_e$ , is

$$\zeta = \frac{2U_e \kappa}{J_0(\kappa R)} \begin{cases} J_1(\kappa r) \sin \theta, & \text{if } r \leq R, \\ 0, & \text{if } r \geq R. \end{cases} \quad (2.10)$$

Above  $r^2 = (x - x_c)^2 + (y - y_c)^2$  is the radial distance about the dipole's center  $(x_c, y_c)$ ,  $\tan \theta = (y - y_c)/(x - x_c)$ , and  $J_n$  is the  $n$ 'th order Bessel function. The matching condition at  $r = R$  is that  $J_1(\kappa R) = 0$  and the smallest solution is  $\kappa R \approx 3.8317$ . If there is no coupling to the wave  $\phi$ , then the dipole (2.10) is a solution of the QG equation (2.7).

We strongly perturb the dipole in (2.10) by seeding a wave with initial velocity:

$$\phi(x, y, t = 0) = \frac{1+i}{\sqrt{2}} U_w. \quad (2.11)$$

If there was no dipole, this initial condition produces a spatially uniform near-inertial oscillation with speed  $U_w$ . Further parameters of this solution are summarized in table 2; note  $U_w = 10U_e$ .

TABLE 2. Description of parameters of Lamb-Chaplygin simulation. The initial condition have Rossby number  $Ro = U_e k_e / f_0 \approx 0.05$ , wave dispersivity  $\hbar = f_0 \lambda^2 k_e / U_e \approx 1$ , and wave amplitude  $\alpha = Ro(U_w/U_e)^2 \approx 3.75$ .

Parameter	Description	Value
$R = 2\pi k_e^{-1}$	Dipole radius	$L_d/15 \approx 84$ km
$U_e$	Dipole strength	$5 \times 10^{-2}$ m s $^{-1}$
$U_w$	NIW speed	$5 \times 10^{-1}$ m s $^{-1}$
$N_0$	Buoyancy frequency	$5 \times 10^{-3}$ s $^{-1}$
$f_0$	Coriolis frequency	$10^{-4}$ s $^{-1}$
$2\pi m^{-1}$	NIW vertical wavelength	325 m
$\kappa_e$	QGPV biharmonic diffusivity	$5 \times 10^7$ m $^4$ s $^{-1}$
$\nu_w$	NIW biharmonic viscosity	$1 \times 10^7$ m $^4$ s $^{-1}$
$N$	Number of modes	512
$L_d$	Domain size	$2\pi \times 200$ km

With the initial condition in (2.11),  $q^w$  in (2.6) and  $\nabla\phi$  are both zero at  $t = 0$ . The refractive term in the wave equation (2.8), however, immediately imprints itself onto  $\phi$  thus creating non-zero  $\nabla\phi$  and non-zero  $q^w$ . Once refraction has created gradients in  $\phi$ , the advective term in (2.8) can further distort  $\phi$  and increase  $\nabla\phi$ . This scale reduction of  $\phi$  is most evident in the wave buoyancy shown in lower row of figure 1. Figure 1 also shows the well-known focussing of waves into the negative vortex. But the wave feedback on the mean flow through  $q^w$  then results in distortion and shearing of the dipole so that the negative vortex loses its integrity; the lop-sided dipole then starts to drift. Once the negative vortex is distorted to small scales it no longer acts as an effective potential well: the trapping of wave energy by the deformed anti-cyclone is weaker than in the initial condition. In fact, figure 1, which shows the materially conserved PV  $q$ , understates the development of small scales in the relative vorticity  $\zeta$ : figure 2 shows that both  $\zeta$  and  $q^w$  develop small scales with significant cancellation resulting in the relatively smooth field  $q = \zeta + q^w$  shown in figure 1. Thus at the final time in figure 1 the waves are no longer strongly trapped in the region with  $\zeta < 0$ . This phenomenology, including significant cancellation between  $\zeta$  and  $q^w$ , is also characteristic of wave-modified two-dimensional turbulence in section 4.

To understand the results in figure 1 and quantify the stimulated generation of wave energy, we need to understand the conservation laws of the vertical plane-wave model.

### 3. Conservation laws of the vertical plane wave model

XV noted that the vertical plane wave model in (2.6) through (2.8) inherits two quadratic conservation laws from the parent NIW-QG model: if there is no dissipation then wave action,

$$\mathcal{A} \stackrel{\text{def}}{=} \frac{|\phi|^2}{2f_0}, \quad (3.1)$$

and the energy,

$$\mathcal{E} \stackrel{\text{def}}{=} \frac{1}{2} |\nabla\psi|^2 + \frac{1}{4} \lambda^2 |\nabla\phi|^2, \quad (3.2)$$

are both separately conserved. Following Bretherton & Garrett (1968), the action in (3.1) is the wave energy divided by the intrinsic frequency; YBJ observed that to leading

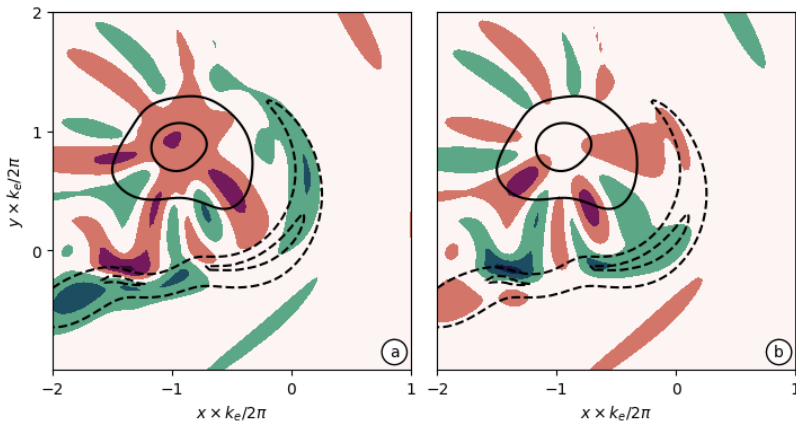


FIGURE 2. (a) Snapshot of  $q$  (contours) and  $\zeta$  (colors) at  $t \times U_e k_e = 20$ . (b) Snapshot of  $q$  (contours) and wave PV  $q^w$  (colors). Both black lines and colors depict the contour levels  $[-1.5, -0.5, 0.5, 1.5] \times (U_e k_e)$ . Solid lines and reddish colors depict positive values; dashed lines and greenish colors show negative values.

order the wave energy is only kinetic and the intrinsic frequency in (3.1) is the inertial frequency  $f_0$ .

The conserved energy density  $\mathcal{E}$  in (3.2) is the sum of the kinetic energy of the balanced flow

$$\mathcal{K} \stackrel{\text{def}}{=} \frac{1}{2} |\nabla \psi|^2, \quad (3.3)$$

and the potential energy of the near-inertial waves,

$$\mathcal{P} \stackrel{\text{def}}{=} \frac{1}{2} b^2 / N_0^2 = \frac{1}{4} \lambda^2 |\nabla \phi|^2. \quad (3.4)$$

Above,  $b \propto \partial \phi$  is the wave buoyancy defined in (2.4). Because  $q^w$  is quadratic in  $\phi$  the conserved enstrophy,  $\langle q^2 \rangle$ , is not a quadratic quantity.

XV explain the physical basis of stimulated generation by noting that balanced kinetic energy  $\mathcal{K}$  can be converted into wave potential energy  $\mathcal{P}$  while conserving the integral of the total energy  $\mathcal{E}$  in (3.2). Indeed, this conversion *must* occur if  $\nabla \phi$  is increased by a combination of refraction and advection in the wave equation (2.8). In the example shown in figure 1, the initial wave field in (2.11) has infinite spatial scale and therefore there is no wave potential energy at  $t = 0$ . The subsequent evolution in figure 1 involves creation of non-zero  $\nabla \phi$ , corresponding to gain of  $\mathcal{P}$  at the expense  $\mathcal{K}$ : this is stimulated generation of near-inertial waves.

To substantiate this intuition, and diagnose results from our simulation of wave modified two-dimensional turbulence, we develop the conservation laws corresponding to (3.1) and (3.2) in more detail.

### 3.1. Action conservation equation and action flux

Multiplying the wave equation (2.8) by  $\phi^*$  and adding to the complex conjugate we obtain a conservation equation for action density

$$\partial_t \mathcal{A} + J(\psi, \mathcal{A}) + \nabla \cdot \mathcal{F} = \frac{\phi^* D_\phi + \phi D_{\phi^*}}{2f_0}, \quad (3.5)$$

where the flux of near-inertial wave action is

$$\mathcal{F} \stackrel{\text{def}}{=} \frac{i}{4} \lambda^2 (\phi \nabla \phi^* - \phi^* \nabla \phi). \quad (3.6)$$

The local conservation law (3.5) shows how the wave action  $\mathcal{A}$  changes due to divergences of the geostrophic and wave fluxes and dissipation—the second, third, and fourth terms in (3.5).

The wave action flux  $\mathcal{F}$  is analogous to the probability current of quantum mechanics (e.g., Landau & Lifshitz 2013, pg. 57). Using the polar representation  $\phi = |\phi|e^{i\Theta}$ , the wave action flux  $\mathcal{F}$  can also be written as

$$\mathcal{F} = \mathcal{A}\eta\nabla\Theta, \quad (3.7)$$

where recall that  $\eta = f_0\lambda^2$  is the dispersivity. In (3.7),  $\eta\nabla\Theta$  is the “generalized group velocity” of hydrostatic near-inertial waves, i.e.,  $\mathcal{F}$  is the generalized group velocity times the action density  $\mathcal{A}$ . We use the term “generalized” because no WKB-type scale separation is required to obtain the results above. The connection to standard internal-wave group velocity is quickly verified by considering a plane near-inertial wave with  $\Theta = kx + ly$ , yielding  $f_0\lambda^2\nabla\Theta = N_0^2(k, l)/f_0m^2$ .

Another useful identity involving the action flux  $\mathcal{F}$  is

$$\nabla \cdot (\hat{\mathbf{k}} \times \mathcal{F}) = \frac{1}{2}\lambda^2 J(\phi^*, \phi), \quad (3.8)$$

where  $\hat{\mathbf{k}}$  is the unit vector perpendicular to the  $(x, y)$ -plane. Using (3.8), and the definition of action in (3.1), the wave PV  $q^w$  in (2.6) can be written as

$$q^w = \frac{1}{2}\triangle\mathcal{A} + \eta^{-1}\nabla \cdot (\hat{\mathbf{k}} \times \mathcal{F}). \quad (3.9)$$

Denoting an average over the domain by  $\langle \rangle$ , and assuming that the action flux divergence  $\nabla \cdot \mathcal{F}$  vanishes after integration, we obtain from (3.5)

$$\frac{d\langle \mathcal{A} \rangle}{dt} = \varepsilon_{\mathcal{A}}. \quad (3.10)$$

where  $\varepsilon_{\mathcal{A}} \stackrel{\text{def}}{=} \langle \phi^* D_\phi + \phi D_{\phi^*} \rangle / (2f_0)$  is the domain average of the dissipative term on the right of (3.5). In the example shown in Figure 1 the total action  $\langle \mathcal{A} \rangle$  is conserved to within 1% over the course of the integration.

### 3.2. Ehrenfest’s theorem

The quantum analogy suggests that we should seek an analog of Ehrenfest’s theorem (the quantum equivalent of Newton’s law that force equals mass times acceleration). Thus in Appendix B we develop a local conservation law for  $\mathcal{F}$ . The domain average of that result is

$$\frac{d\langle \mathcal{F} \rangle}{dt} = \hat{\mathbf{k}} \times \langle \zeta \mathcal{F} \rangle - \langle \mathcal{A} \nabla \frac{1}{2} \zeta \rangle + \varepsilon_{\mathcal{F}}. \quad (3.11)$$

In the quantum analogy,  $\mathcal{F}$  is momentum and the left hand side of (3.11) is mass times acceleration; the forces are on the right of (3.11). Starting from the end,  $\varepsilon_{\mathcal{F}}$  is a dissipative term defined in Appendix B. The second term on the right of (3.11) is the force due to the gradient of the potential  $\zeta/2$ . The first term on the right of (3.11) is a “vortex force,” again due to  $\zeta$ , but perpendicular to  $\mathcal{F}$ ; the vortex force lacks a quantum analog.

The results in this section are obtained from the wave equation (2.8) without using the QGPV equation (2.7). In other words, (3.5)–(3.11) apply to the YBJ equation with  $e^{imz}$  structure regardless of the balanced-flow dynamics. We turn now to energy conservation and consideration of the QGPV equation (2.7).

### 3.3. Energy conservation and energy conversion

The energy conservation law is considerably more complicated than action conservation. We sequester the details of the local conservation laws to Appendix B and present



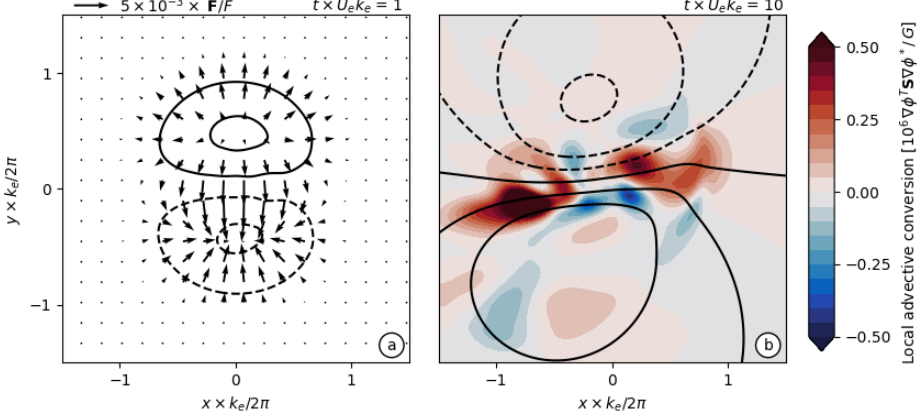


FIGURE 3. Illustration of energy conversion terms in the Lamb-Chaplygin dipole solution with parameters presented in table 2. (a) The action flux  $\mathcal{F}$  overlain on contours of relative vorticity  $\Delta\psi/(U_e k_e) = [-1.5, -0.5, 0.5, 1.5]$ , with dashed lines showing negative values; the scale of the action flux is  $F = f_0 \lambda^2 k_e U_w^2$ . (b) The local advective conversion (i.e., the unaveraged  $\Gamma_a$ ) overlain on contours of streamfunction  $\psi \times (U_e/k_e) = [-8, -4, -2, 0, 2, 4, 8]$ .

here the simpler results obtained by domain averaging those local conservation laws. For the wave potential energy in (3.4) and the balanced kinetic energy in (3.3) we find

$$\frac{d\langle \mathcal{P} \rangle}{dt} = \Gamma_r + \Gamma_a + \varepsilon_{\mathcal{P}}, \quad (3.12)$$

$$\frac{d\langle \mathcal{K} \rangle}{dt} = -\Gamma_r - \Gamma_a + \Xi + \varepsilon_{\mathcal{K}}, \quad (3.13)$$

where the “conversion terms” in (3.12) and (3.13) are

$$\Gamma_r \stackrel{\text{def}}{=} \left\langle \frac{1}{2} \zeta \nabla \cdot \mathcal{F} \right\rangle, \quad (3.14)$$

and

$$\Gamma_a \stackrel{\text{def}}{=} -\frac{\lambda^2}{2} \left\langle \begin{bmatrix} \phi_x^* & \phi_y^* \end{bmatrix} \begin{bmatrix} -\psi_{xy} & \frac{1}{2}(\psi_{xx} - \psi_{yy}) \\ \frac{1}{2}(\psi_{xx} - \psi_{yy}) & \psi_{xy} \end{bmatrix} \begin{bmatrix} \phi_x \\ \phi_y \end{bmatrix} \right\rangle. \quad (3.15)$$

The dissipative terms,  $\varepsilon_{\mathcal{P}}$ ,  $\varepsilon_{\mathcal{K}}$  and  $\Xi$  are defined in appendix B.  $\Xi$  in (3.13) is particularly interesting: dissipation of waves  $D_\phi$  produces balanced kinetic energy. Summing (3.12) and (3.13) the “conversion” terms  $\Gamma_r$  and  $\Gamma_a$  cancel, and we obtain the conservation law for total energy  $\langle \mathcal{E} \rangle = \langle \mathcal{P} + \mathcal{K} \rangle$ .

The refractive conversion  $\Gamma_r$  stems from  $i\phi\zeta/2$  in the wave equation and is easy to interpret: the convergence of the wave action flux,  $\nabla \cdot \mathcal{F} < 0$ , into anti-cyclones,  $\zeta < 0$ , is a source of wave potential energy  $\mathcal{P}$ . Figure 3a shows the convergence of  $\mathcal{F}$  into the anti-cyclone (and divergence from the cyclone) of the dipole solution at  $t \times U_e k_e = 1$ , which yields the sharp initial increase of  $\langle \mathcal{P} \rangle$  discussed below. Ehrenfest’s theorem in (3.11) illuminates the initial structure of  $\mathcal{F}$  in figure 3. Because  $\phi$  is initially uniform, the initial tendency of  $\langle \mathcal{F} \rangle$  is

$$\partial_t \langle \mathcal{F} \rangle \approx -\eta \langle \mathcal{A} \nabla \cdot \frac{1}{2} \zeta \rangle. \quad (3.16)$$

Thus, on average, the action flux is initially anti-parallel to the gradient of relative vorticity; figure 3 shows that in the dipole example this result holds point-wise.

The advective conversion  $\Gamma_a$  in (3.12) and (3.13) stems from the term  $J(\psi, \phi)$  in the wave equation (2.8) and is a source of  $\langle \mathcal{P} \rangle$  due to straining and deformation of the wave

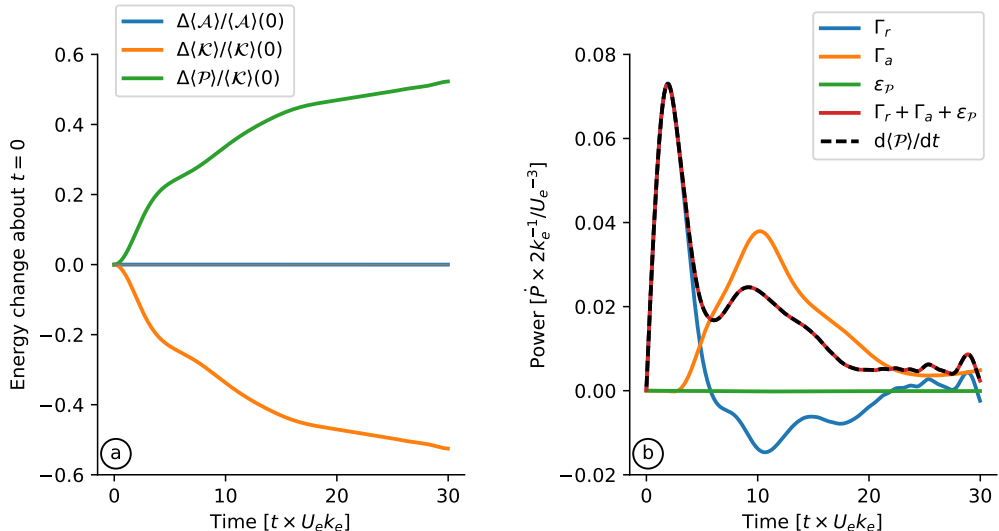


FIGURE 4. Diagnostics of the Lamb-Chaplygin dipole solution with parameters presented in table 2. (a) Energy change about initial condition. (b) Wave potential energy budget (3.12).

field by the geostrophic flow. The symmetric  $2 \times 2$  matrix in (3.15) is the strain or deformation tensor of the geostrophic flow. Thus, in analogy with passive scalar gradient amplification, straining also enhances gradients of the back-rotated near inertial velocity  $\phi$ , thereby generating wave potential energy  $\langle\mathcal{P}\rangle$ .

### 3.4. Energetics of the Lamb-Chaplygin dipole solution

Figure 4 shows the energetics of the Lamb-Chaplygin dipole solution in figure 1. In figure 4a,  $\mathcal{P}$  increases at the expense of  $\mathcal{K}$ , while  $\mathcal{A}$  is conserved. The wave potential energy budget in figure 4b shows that this stimulated generation occurs in two stages. First, refraction of the initially uniform wave field causes a dramatic concentration of waves into the anti-cyclone producing a sharp increase  $\mathcal{P}$  through  $\Gamma_r$ . But this rapid initial energy conversion does not last long because the wave feedback deforms the anti-cyclone and dispersion radiates waves away from the dipole (see figure 1). Thus in figure 4b,  $\Gamma_r$  decreases sharply, and eventually reverses sign at  $t \times U_e k_e \approx 8$ .

The second stage of stimulated generation in the dipole solution starts after refraction has created dipole-scale waves. Advection by the balanced flow can then strain the waves, further reducing their lateral scale (figure 4b). The ensuing advective conversion,  $\Gamma_a$ , starts at  $t \times U_e k_e \approx 4$ . Straining by the balanced flow sustains this advective generation of  $\mathcal{P}$ . The waves eventually escapes the straining regions through dispersion and the conversion nearly halts at  $t \times U_e k_e = 30$ . The time-integrated  $\Gamma_a$  accounts for  $\approx 78\%$  of the wave potential energy generation; table 3 summarizes the energy budget.

### 3.5. Summary

The expressions for energy conversion in (3.14) and (3.15) clarify the mechanism of stimulated generation triggered by the initially uniform near-inertial wave in (2.11). First, refraction causes a convergence of wave action into anti-cyclones. Then advection strains the waves, reducing their lateral scale. Both processes amplify the lateral gradients of wave amplitude, thereby generating wave potential energy  $\mathcal{P}$  at the expense of balanced kinetic energy  $\mathcal{K}$ . Wave action  $\mathcal{A}$  is conserved throughout this process.

TABLE 3. The time-integrated budget of wave potential energy and quasigeostrophic kinetic energy of the Lamb-Chaplygin dipole solutions with parameters provided in table 2. The energy budgets close within  $10^{-6}$  %.

$\dot{P}_w$ budget	Fractional size ( $\int \dot{P}_w dt / \Delta P_w$ )	$\dot{K}_e$ budget	Fractional size ( $\int \dot{K}_e dt / \Delta K_e$ )
$\Gamma_r$	0.228	$-\Gamma_r$	-0.227
$\Gamma_a$	0.778	$-\Gamma_a$	-0.774
—	—	$\Xi_r$	0.004
—	—	$\Xi_a$	0.0
$\chi_\phi$	-0.006	$\epsilon_\psi$	-0.003
Res.	0.0	Res.	0.0

In the remainder of this paper, we describe and quantify stimulated generation in an idealization of an oceanographic post-storm scenario: the uniform initial near-inertial wave in (2.11) interacts with two-dimensional turbulence.

#### 4. Macroturbulence modified by near-inertial waves

To study the energy exchange between near-inertial geostrophic flow in an oceanographic turbulent regime, we consider a barotropic flow that emerges from random initial conditions integrated for 20 eddy turnover time units. In other words, we first integrate the initial condition

$$\psi(x, y, t \times U_e k_e = -20) = \sum_{k,l} \psi_{\mathbf{k}} \cos(kx + ly + \chi_{\mathbf{k}}) \quad (4.1)$$

with waveless QG dynamics before introducing the wave in (2.11) at  $t \times U_e k_e = 0$ . Above,  $\chi_{\mathbf{k}}$  is a random phase uniformly distributed on  $[0, 2\pi)$ , and  $\psi_{\mathbf{k}}$  is the streamfunction isotropic spectrum

$$\psi_{\mathbf{k}} = C \times \{|\mathbf{k}| [1 + (|\mathbf{k}|/k_e)^4]\}^{-1/2}, \quad (4.2)$$

with the wavenumber magnitude  $|\mathbf{k}|^2 = k^2 + l^2$ . The prescribed initial energy  $U_e^2/2$  determines the constant  $C$ :

$$\sum_{k,l} \underbrace{|\mathbf{k}|^2 \psi_{\mathbf{k}}^2}_{\stackrel{\text{def}}{=} \mathcal{K}_e} = \frac{1}{2} U_e^2. \quad (4.3)$$

The kinetic energy spectrum,  $\mathcal{K}_e$ , peaks at the energy-containing scale  $k_e^{-1}$ . At scales larger than  $k_e^{-1}$ ,  $\mathcal{K}_e$  has a linear dependence on  $|\mathbf{k}|$ , whereas  $\mathcal{K}_e$  decays as  $|\mathbf{k}|^{-3}$  at scales smaller than  $k_e^{-1}$ . This red spectrum ensures insignificant loss of energy by small-scale dissipation  $D_q$  in (2.7).

The evolution of a random initial condition under quasi-inviscid QG dynamics (2.7) has been well studied, beginning perhaps with [Fornberg \(1977\)](#). Stirring of vorticity  $\Delta\psi$  transfers enstrophy towards small scales; energy flows to large scales. Most of enstrophy is dissipated within few eddy turnover times, whereas kinetic energy is nearly conserved. Vorticity concentrates into localized coherent structures: after 20 eddy turnover time units, the vorticity is well-organized into an ensemble of vortices that form via like-sign vortex merging (e.g., [McWilliams 1984](#)).

TABLE 4. Description of parameters of the macroturbulence simulations. The initial condition have Rossby number  $Ro = U_e k_e / f_0 \approx 0.05$ , wave dispersivity  $\hbar = f_0 \lambda^2 k_e / U_e \approx 0.5 - 2$ , and wave amplitude  $\alpha = Ro(U_w / U_e)^2 \approx 0.2$ .

Parameter	Description	Value
$R = 2\pi k_e^{-1}$	Energy-containing scale	$L_d/10 \approx 125$ km
$U_e$	Eddy velocity	$5 \times 10^{-2}$ m s $^{-1}$
$U_w$	NIW speed	$1 \times 10^{-1}$ m s $^{-1}$
$N_0$	Buoyancy frequency	$5 \times 10^{-3}$ s $^{-1}$
$f_0$	Colioris frequency	$10^{-4}$ s $^{-1}$
$2\pi m^{-1}$	NIW vertical wavelength	280 – 560m
$\kappa_e$	QGPV biharmonic diffusivity	$5 \times 10^6$ m $^4$ s $^{-1}$
$\nu_w$	NIW biharmonic viscosity	$5 \times 10^6$ m $^4$ s $^{-1}$
$N$	Number of modes	1024
$L_d$	Domain size	$2\pi \times 200$ km

TABLE 5. The time-integrated budget of wave potential energy and QG kinetic energy of the reference macroturbulence solution with parameters in 4. The energy budgets close within 0.1 %.

$\dot{P}_w$ budget	Fractional size ( $\int \dot{P}_w dt / \Delta P_w$ )	$\dot{K}_e$ budget	Fractional size ( $\int \dot{K}_e dt / \Delta K_e$ )
$\Gamma_r$	0.117	$-\Gamma_r$	-0.108
$\Gamma_a$	0.907	$-\Gamma_a$	-0.839
—	—	$\Xi_r$	0.009
—	—	$\Xi_a$	0.003
$\chi_\phi$	-0.026	$\epsilon_\psi$	-0.062
Res.	0.003	Res.	0.003

#### 4.1. Relevant parameters

The scaling

$$\text{length} \sim k_e^{-1}, \quad \text{time} \sim (U_e k_e)^{-1}, \quad \psi \sim U_e k_e^{-1}, \text{ and } \quad \phi \sim U_w, \quad (4.4)$$

shows that there are two important dimensionless control parameters. The first is

$$\alpha \stackrel{\text{def}}{=} \underbrace{\frac{U_e k_e}{f_0}}_{\stackrel{\text{def}}{=} Ro} \times \left( \frac{U_w}{U_e} \right)^2, \quad (4.5)$$

which measures the strength of the waves compared to the geostrophic flow and scales the contribution of the wave terms in the potential vorticity (2.6). The second dimensionless parameter is

$$\hbar \stackrel{\text{def}}{=} \eta \times \frac{k_e}{U_e}, \quad (4.6)$$

which scales wave dispersion against the effects of advection and refraction.

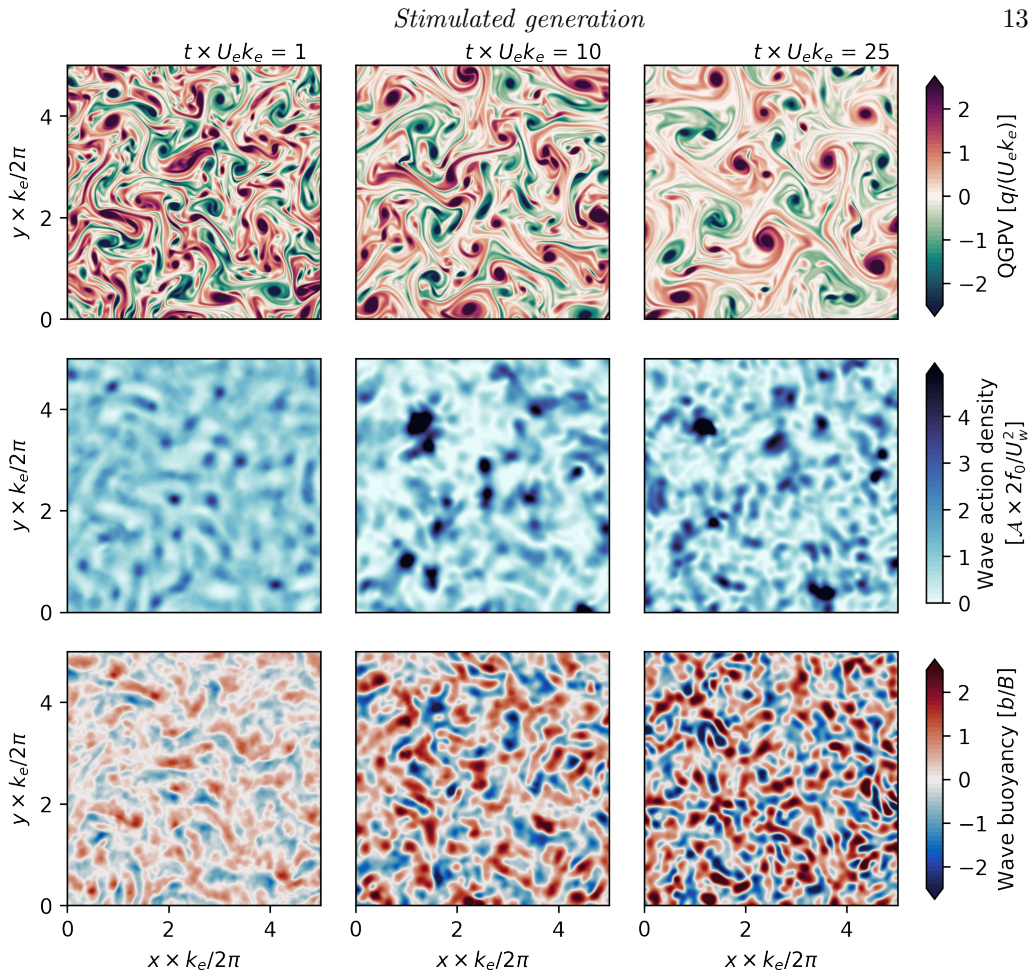


FIGURE 5. Snapshots of the turbulence solution with parameters in table 4. Upper panels: QGPV. Middle panels: wave kinetic energy density  $|\phi|^2$ . Bottom panels: wave buoyancy, with scale  $B = k_e m U_w f_0 \lambda^2$ . These plots show  $(1/2)^2$  of the domain.

#### 4.2. Solution with $\hbar = 1$ and $\alpha = 0.1$

Figure 5 show snapshots of a solution with  $\hbar = 1$  and  $\alpha = 0.1$  and further parameters in table 4. This turbulence solution shares qualitative aspects of the Lamb-Chaplygin solution. Starting from a uniform wave field in (2.11), refraction quickly concentrates the waves into anti-cyclones. By  $t \times U_e k_e \approx 1$  there is a two-fold modulation of the wave action density on eddy scales with significant focussing of waves in anti-cyclones (compare middle and upper panels of figure 5).

Dispersion radiates waves from the vortices; advection enhances the gradients of back-rotated velocity  $\phi$  (see lower panels of figure 5, which depict wave buoyancy). By  $t \times U_e k_e \approx 10$  there is a five-fold modulation of the wave kinetic energy density and the wave buoyancy has been amplified by a factor of two. The evolution of potential vorticity  $q$  is similar to that in the waveless problem: like-sign vortices merge into bigger vortices. The big vortices keep straining the waves, generating smaller scales in the wave field.

Figure 6a shows the inexorable increase in wave potential energy  $\langle \mathcal{P} \rangle$  and the corresponding decrease in balanced kinetic energy  $\langle \mathcal{K} \rangle$ . In figure 6b quick wave refraction results in an initial sharp generation of  $\langle \mathcal{P} \rangle$  at the expense of balanced kinetic energy

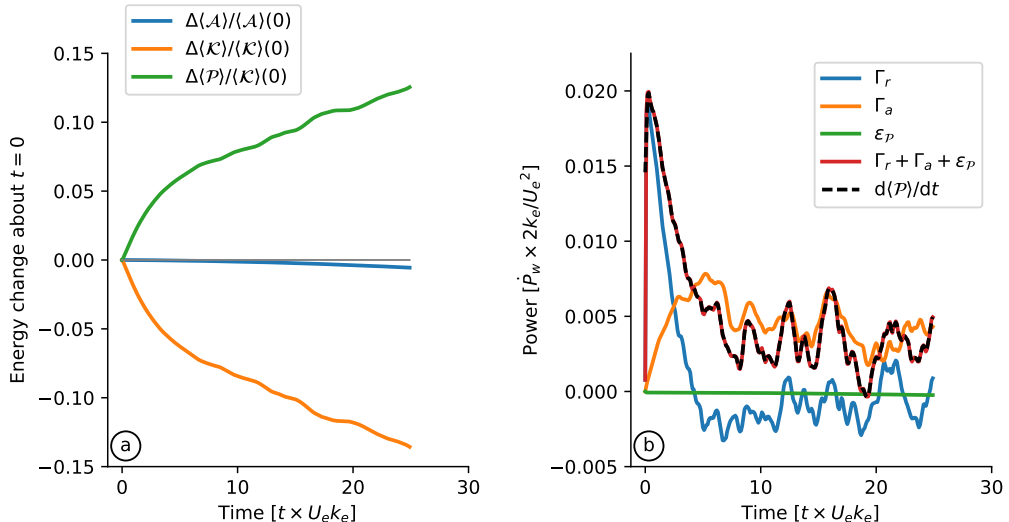


FIGURE 6. Diagnostics of the macroturbulence solution with parameters presented in table 4. (a) Energy change about initial condition. (b) Wave potential energy budget (3.12).

$\langle\mathcal{K}\rangle$ . As in the Lamb-Chaplygin solution, the positive refractive conversion,  $\Gamma_r > 0$ , is ephemeral: in figure 6b,  $\Gamma_r$  peaks at  $t \times U_e k_e \approx 2$  and then decays rapidly, eventually changing sign at  $t \times U_e k_e \approx 5$ . But a significant positive advective conversion,  $\Gamma_a > 0$ , sustains stimulated generation so that  $\langle\mathcal{P}\rangle$  ultimately increases approximately linearly with time.

After 25 eddy-turnover time units, the balanced kinetic energy  $\langle\mathcal{K}\rangle$  has decayed by about 14% from its initial value. Most of this loss is by stimulated generation of  $\langle\mathcal{P}\rangle$ . As in the Lamb-Chaplygin solution, advective conversion accounts for most of the energy change. Table 5 presents further details of the energy budget.

The solution illustrates interesting characteristics of stimulated generation. First, the role of refraction is catalytic in that it generates the initial eddy-scale gradients in  $\phi$  that are then enhanced by advective straining; the advective conversion,  $\Gamma_a$  in (3.15), ultimately accounts for most of the energy transfer from turbulence to waves. Second, the roughly linear-in-time growth of wave potential energy  $\langle\mathcal{P}\rangle$  is very slow in comparison with exponential increase of passive-scalar tracer gradients in turbulent velocity fields. The relatively slow growth of  $\langle\mathcal{P}\rangle$  suggests that wave dispersion plays an important role in slowing and perhaps opposing advective straining (see section 5 for further discussion of dispersion and “wave escape”). To investigate whether these characteristics are general we consider solution with varying vertical wavelengths and therefore different dispersivities.

#### 4.3. Varying dispersivity

Figure 7 shows snapshots of potential vorticity  $q$  and its constituents in a set of solutions with varying the vertical wavelength  $2\pi m^{-1}$  from 280 to 560 m, yielding dispersivities ranging from 0.5 to 2. (All other parameters are fixed.) The potential vorticity  $q$  shows more small-scale filamentation with decreasing dispersivity, but it is otherwise remarkably similar across the three solutions. The partition into relative vorticity  $\Delta\psi$  and wave potential vorticity  $q^w$ , however, depends significantly on dispersivity. In particular,  $q^w$  develops smaller scales and larger amplitudes with decreasing dispersivity. As anticipated by the dipole example in figure 2, there is cancellation of small-scale



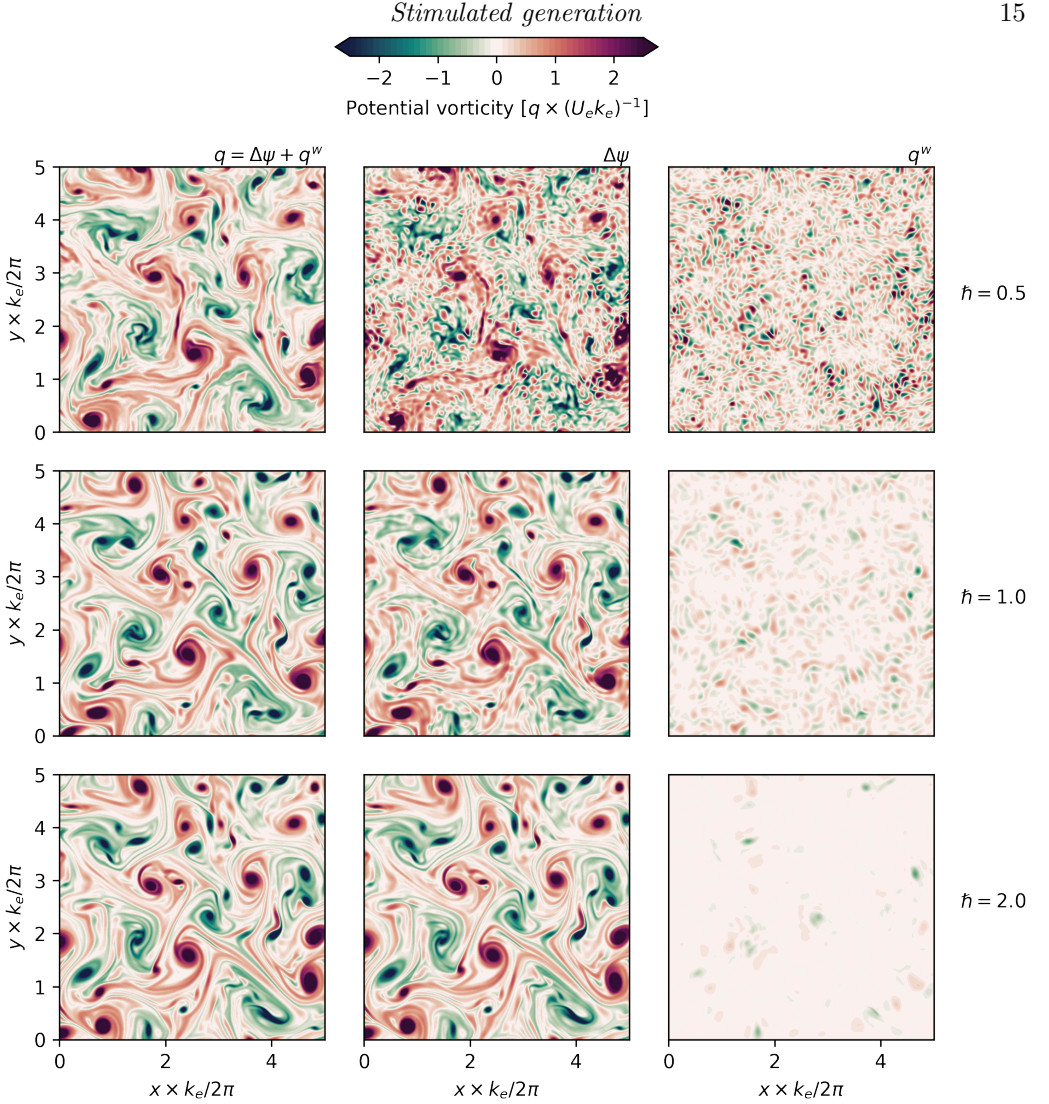


FIGURE 7. Snapshots of QGPV  $q$  and its decomposition into relative vorticity  $\zeta = \Delta\psi$ , and wave potential vorticity  $q^w$ . The snapshots were taken at  $t \times U_e k_e = 25$ .

features in  $q^w$  against those in  $\zeta$  so that  $q$  is relatively smooth even in the solution with weak dispersion  $\hbar = 0.5$ .

The initial evolution of the uniform wave field is similar across dispersivities, with refraction initially generating eddy-scale gradients of the waves—see figure 8. Refraction produces a sharp initial increase of wave potential energy and decrease of balanced kinetic energy, which is almost independent of dispersivity. Figure 9a shows that this initial “refractive stage” yields a strongly negative wave-vorticity correlation  $r$ ,

$$r \stackrel{\text{def}}{=} \frac{\langle \zeta \mathcal{A}' \rangle}{\sqrt{\langle \zeta^2 \rangle \langle \mathcal{A}'^2 \rangle}}, \quad (4.7)$$

where  $\mathcal{A}' \stackrel{\text{def}}{=} (|\phi|^2 - |\langle \phi \rangle|^2)/f_0$ ; in figure 9a the initial negative  $r$  is nearly independent of dispersivity. Because significant energy exchange takes place in the anti-cyclones due to the initial wave concentration, a positive vorticity skewness ensues (figure 9b). Once the

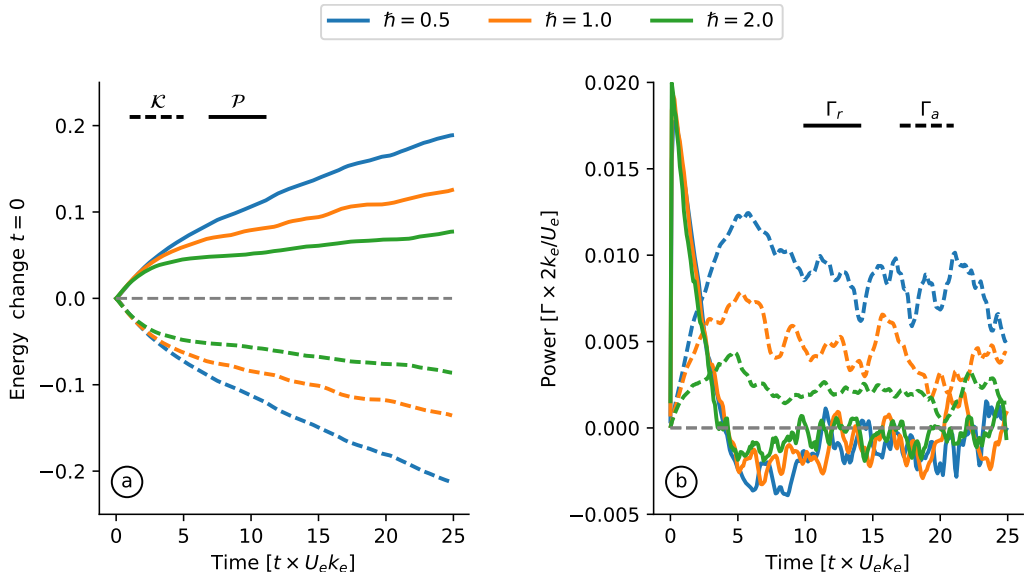


FIGURE 8. The energetics of macroturbulence solutions with different dispersivities. (a) Energy change about the initial condition. (b) The energy conversion terms in (3.12).

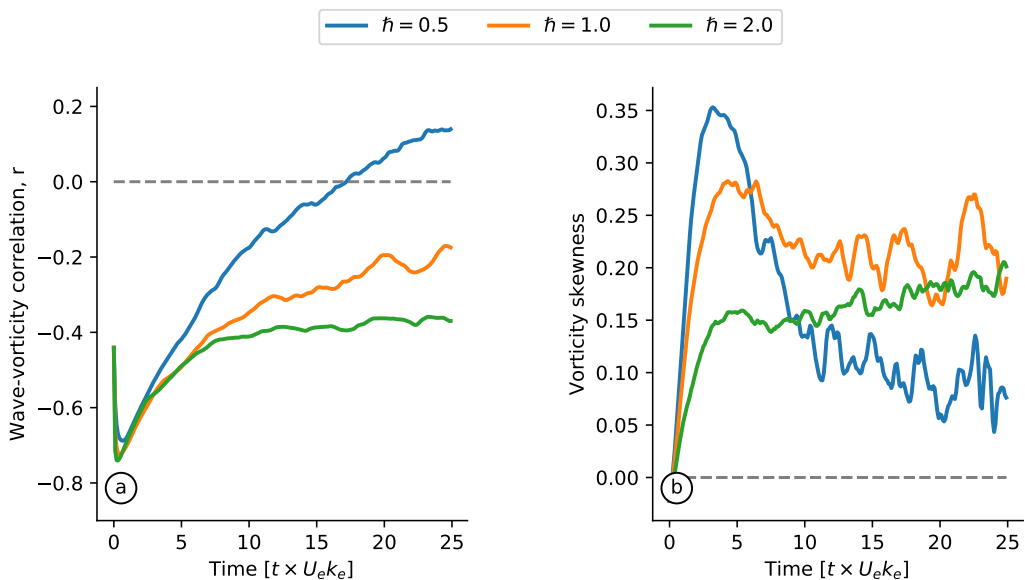


FIGURE 9. Diagnostics of macroturbulence solutions with different dispersivities. (a) The correlation between relative vorticity and wave kinetic energy. (b) The skewness of relative vorticity.

eddy-scales are created, advection strains the waves and generates further wave potential energy at the expense of balanced kinetic energy. It is in this stage that the dependence on dispersivity is pronounced: weakly dispersive waves are strained further than strongly dispersive waves. Thus the advective conversion becomes stronger with decreasing dispersivity (figure 8b). Advection and dispersion significantly reduces the wave-vorticity correlation; the reduction in correlation increases as the dispersivity decreases (figure 9a).



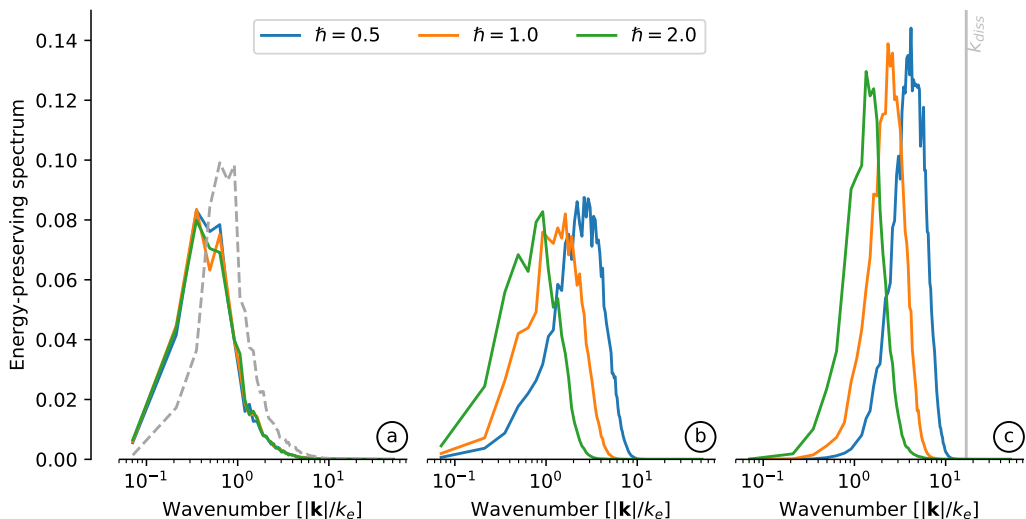


FIGURE 10. Energy-preserving spectra of macroturbulence solutions with different dispersivities. The three panels show spectra of (a) balanced kinetic energy  $\mathcal{K}$ , (b) wave action  $\mathcal{A}$ , and (c) wave potential energy  $\mathcal{P}$ . All solid lines correspond to spectra at  $t \times U_e k_e = 25$  and the dashed line in (a) is the balanced kinetic energy spectrum at  $t \times U_e k_e = 0$ .

For the weakest dispersivity considered, the wave-vorticity correlation becomes weakly positive likely because of the initial positive vorticity skewness.

In all solutions reported above, the evolution of the balanced flow is similar to that of waveless macroturbulence: there is a transfer of balanced energy towards larger scales driven by merger of like-signed vortices—see figure 10a. The main difference is that balanced kinetic energy is not conserved; kinetic energy is constantly transformed into wave potential energy via stimulated generation. The stimulated generation process is associated with a forward transfer of wave action  $\mathcal{A}$  from the infinite horizontal scale in the initial condition (2.11) to the eddy scale; see figure 10b. The wave potential energy density  $\mathcal{P}$  in figure 10c develops significantly smaller scales than those of the balanced kinetic energy  $\mathcal{K}$  in figure 10a.

## 5. Discussion and conclusions

The expression for the energy conversion in (3.12) illuminates the physics of stimulated generation: both convergence of wave action density into anti-cyclones (3.14) and geostrophic straining of the wave field (3.15) are sources of wave potential energy and sinks of balanced kinetic energy. But this characterization of stimulated generation ignores the important role of wave dispersion—waves can propagate out of the vorticity or straining regions, thereby reducing the correlations  $\Gamma_r$  and  $\Gamma_a$  required for stimulated generation.

### 5.1. Wave escape

Wave dispersion is indeed the only mechanism that upsets stimulated generation in the quasi-inviscid solutions described in this paper. In all solutions, after an initial conversion due to refraction, advective straining accounts for most of the energy conversion. Experience with the passive-scalar problem suggests (incorrectly) that the wave potential energy  $\mathcal{P}$  should then increase exponentially with time as  $\nabla\phi$  is amplified by stirring

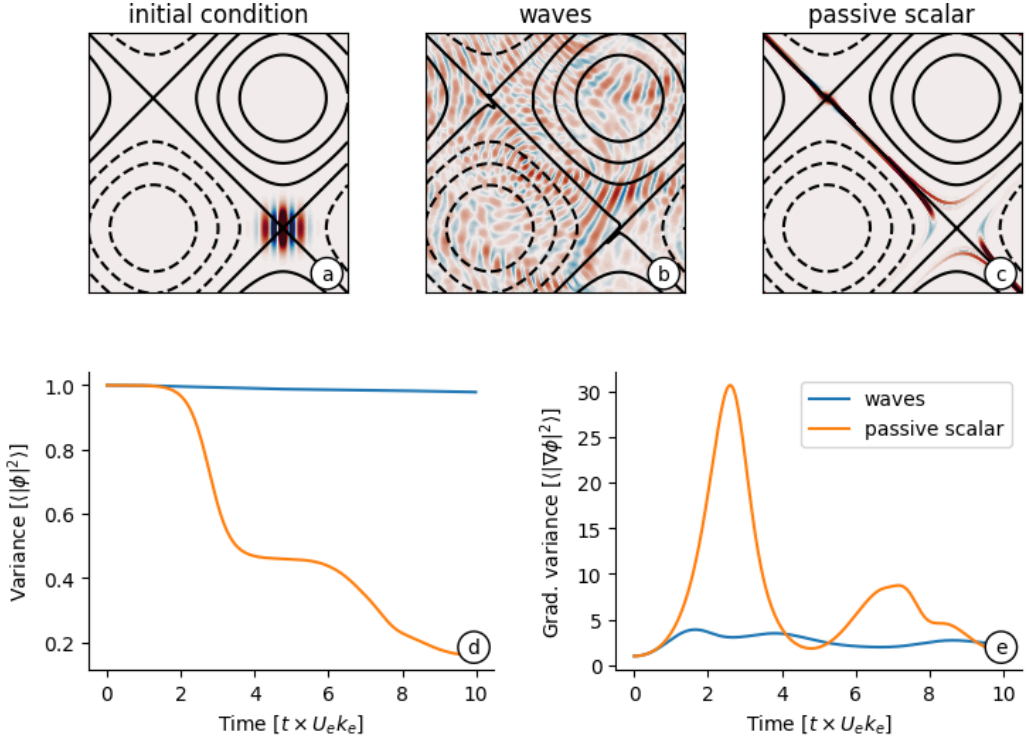


FIGURE 11. A comparison of passive-scalar and wave solutions ( $\hbar \approx 0.09$ ) with same initial conditions (the wave kinetic energy is equal the passive-scalar variance) and same small-scale dissipation. (a) Initial condition of wave back-rotated zonal velocity and of the passive scalar. (b) Wave back-rotated zonal velocity at  $t \times U_e k_e = 10$ . (c) Passive-scalar concentration at  $t \times U_e k_e = 10$ . (d) Variance of wave velocity or passive-scalar variance. (e) Variance of wave velocity gradient or passive scalar. In (d) and (e), the diagnostics are normalized by their initial values.

(e.g., [Young et al. 1982](#)). But even in the weakly dispersive limit, the waves do not behave as a passive scalar (see figure 8) and stimulated generation is much less effective than suggested by this “passive-scalar thinking.” This is because advective straining can only increase  $\nabla\phi$  so much: the near-inertial generalized group velocity is  $\eta\nabla\Theta$  (cf. section 3), where  $\Theta$  is the phase of the near-inertial back-rotated velocity  $\phi = |\phi|e^{i\Theta}$ . Geostrophic straining enhances  $\nabla\Theta$  thereby increasing the near-inertial group velocity so that the waves escape the straining region. Thus, straining by a barotropic balanced flow results in near-inertial “wave escape,” as opposed to the “wave capture” described by [Bühler & McIntyre \(2005\)](#). Indeed, wave capture requires *both* lateral strain *and* vertical shear: the vertical plane wave model has no vertical shear and therefore wave capture is inoperative; see [Thomas \(2012\)](#) for further discussion of the importance of vertical shear to wave capture.

We are surprised by the successful resistance mounted by the waves to strain-driven exponential amplification of  $\nabla\phi$  and thus seek to illustrate wave escape with a simple flow. Figure 11 shows the escape of a wave packet initially placed at the saddle point of a large-scale balanced flow with  $\psi \propto \sin x + \sin y$ . The behavior of the wave packet is qualitatively different from that of a passive scalar in the same flow. The passive scalar packet is strained until it is diffused into oblivion. On the other hand, the waves are strained just so much, resulting in acceleration and escape from the straining region; the

waves finally concentrate in the regions with non-zero vorticity, i.e., in the regions where the Okubo-Weiss criterion indicates no exponential stretching. The top row of figure 11 depicts this striking difference between the behavior of passive scalar and waves. In the bottom row, figure 11d shows that while wave action  $\propto |\phi|^2$  is nearly conserved, the analogous passive-scalar variance is nearly fully dissipated. Figure 11e shows that the variance of the passive-scalar gradient at first increases exponentially due to straining and then decays due to diffusion. On the other hand, the potential energy of the waves  $\propto |\nabla\phi|^2$  increases slowly and then oscillates around an equilibrium level. The wave-escape phenomenology in the turbulence solutions of section 4 qualitatively resembles that seen in this simple flow. In particular, the wave potential energy does not reach the dissipative scale (figure 10c).

### 5.2. Absence of a direct cascade of wave energy

The solutions reported here introduce the waves at  $t = 0$  in (2.11) with infinite spatial scale. Wave refraction,  $i\phi\zeta/2$  in (2.8), immediately transfers wave energy to the smaller scales of the balanced relative vorticity  $\zeta$ . This giant leap across wavenumbers is not a direct cascade of wave energy in the sense of Kolmogorov. In fact, because of wave escape, the wave energy that is efficiently transferred to eddy scales by refraction does not suffer a turbulence-driven direct cascade to the small length scales at which the dissipation (2.9) is effective. This conclusion hinges on the assumption of a barotropic balanced flow: there still remains the possibility of a direct cascade of wave energy if the balanced flow has vertical shear. If the waves can be coerced into a direct-cascade to small scales then stimulated generation would be stronger than in the vertical plane-wave model.

### 5.3. Regimes of wave-modified turbulence

Geostrophic straining accounts for most of the stimulated generation of wave energy in the examples considered in this paper. But refraction plays a fundamental role in these solutions with the uniform (laterally coherent) initial wave velocity in (2.11) because refraction creates the initial gradients of wave velocity that are then enhanced by geostrophic straining. We experimented by changing the initial condition of  $\phi$  to an eddy-scale plane wave and repeated all the macroturbulence solutions; the different initial condition significantly suppresses the initial refraction stage, but otherwise yields long-term solutions that are qualitatively similar to the solutions discussed above. Thus, to the extent that the uniform-wave initial condition (2.11) idealizes the generation of large-scale upper-ocean inertial oscillations by storms (e.g., Moehlis & Llewellyn Smith 2001; Danioux *et al.* 2015), the initial refraction is a loss of lateral coherence, or a type of inertial pumping (Young & Ben Jelloul 1997; Klein *et al.* 2004), which is accompanied by an extraction of energy from the balanced flow by the waves.

Although 10-20% of the balanced kinetic energy is converted into wave potential energy, and despite the wave breakage of the symmetry between cyclones and anti-cyclones, the wave-modified turbulence in section 4 remarkably resembles waveless two-dimensional turbulence (e.g., McWilliams 1984): we still observe robust vortices and an increase in vortex length scale due to merger of like-signed vortices. Figure 7 shows small changes in the potential vorticity  $q$  and much larger changes in the wave PV  $q^w$  induced by changing the dispersivity. In this sense, the turbulent evolution is insensitive to wave modification.

To see significant wave modification of the turbulence we increased the amplitude of the initial wave in (2.11) so that  $U_w = 6U_e$  (in section 4,  $U_w = 2U_e$ ). With this level of wave energy the wave-modified macroturbulence differs qualitatively from the waveless variety (not shown). The potential vorticity develops highly filamentary structures with little

vortex formation; this inhibition of vortex formation is stronger in the weakly dispersive limit. But this large amplitude, weakly dispersive case is probably irrelevant to ocean dynamics.

#### 5.4. The correlation of wave amplitude with relative vorticity

A secondary result here is the strong time-dependence of the correlation  $r$ , defined in (4.7), between incoherent waves and the relative vorticity;  $r$  measures the concentration of waves into cyclones or anti-cyclones (Danioux *et al.* 2015). Refraction concentrates waves into anti-cyclones and expels them from cyclones, thereby generating an initial strong negative  $r$  (see figure 9a). As conjectured by Danioux *et al.* (2015), the subsequent return of  $r$  towards zero (and even to positive values in the case  $\hbar = 0.5$ ) is partially due to the unsteady geostrophic advection. The NIW-QG coupling compounds the unsteady advection: the dramatic initial concentration of waves into anti-cyclones weakens those vortices, with ensuing development of positive skewness of relative vorticity (see figure 9b); the vorticity skewness increases with decreasing dispersivity because weakly dispersive waves extract more balanced kinetic energy (see figure 8).

#### 5.5. Final remarks

There are many caveats to the application of our results to the post-storm oceanographic problem. Notably, the lack of geostrophic vertical shear suppresses important mechanisms of vertical refraction and straining, which introduce interesting modifications of the near-inertial wave physics (e.g., Thomas 2012) and can account for copious energy extraction by near-inertial waves (Shakespeare & Hogg 2017). Furthermore, our focus on quasi-inviscid initial value problems downplays the role of dissipation; in forced-dissipative solutions, wave dissipation likely controls the strength of stimulated generation. We hope to explore these effects in future work.

This study was supported by the National Aeronautics and Space Administration (NNX16AO5OH) and the National Science Foundation (OCE1357047).

## Appendix A. Details of the NIW-QG model

Using multiscale asymptotic theory, Wagner & Young (2016) derive a model for the coupled evolution of QG balanced flow, near-inertial waves and their second harmonic. Assuming that the second harmonic is zero ( $B = 0$  in Wagner & Young), the Wagner & Young (2016) coupled model recovers the XV model in the limit where the waves have vertical scales much smaller than the balanced flow. The coupled model is asymptotic in wave amplitude

$$\epsilon \stackrel{\text{def}}{=} \frac{U_w}{f_0 L} \ll 1, \quad (\text{A } 1)$$

where  $L$  is a characteristic scale of both waves and balanced flow, and it assumes that the balanced flow is weak, specifically  $U_e = \epsilon U_w$  so that

$$Ro \stackrel{\text{def}}{=} \frac{U_e}{f_0 L} = \epsilon^2. \quad (\text{A } 2)$$

In Wagner & Young (2016), the QGPV is

$$q = (\Delta + L)\psi + \beta y + \frac{1}{f_0} \left[ \Delta \frac{1}{2} |LA|^2 + J(LA^*, LA) \right], \quad (\text{A } 3)$$

where  $\Delta \stackrel{\text{def}}{=} \partial_x^2 + \partial_y^2$  and  $L \stackrel{\text{def}}{=} \partial_z (f_0/N)^2 \partial_z$ , and  $LA$  is the back-rotated near-inertial velocity; the total velocity is

$$u + iv = LAe^{-if_0 t} - \psi_y + i\psi_x. \quad (\text{A } 4)$$

The QGPV is materially conserved,

$$q_t + J(\psi, q) = 0, \quad (\text{A } 5)$$

and the wave back-rotated velocity satisfies the YBJ equation,

$$LA_t + \frac{i}{2}f_0\Delta A + J(\psi, LA) + iLA(\frac{1}{2}\Delta\psi + \beta y) = 0. \quad (\text{A } 6)$$

The special family of solutions with barotropic balance flow  $\psi = \psi(x, y, t)$ ,  $f$ -plane ( $\beta = 0$ ), uniform background buoyancy frequency  $N = N_0$ , and  $LA = e^{imz} \phi(x, y)$  wave velocity yields the vertical plane wave model in (2.7)-(2.8). The plane wave model is a solution of both XV and [Wagner & Young \(2016\)](#) equations because the barotropic flow assumption yields an infinite vertical-scale separation between waves and balanced flow.

We solve the vertical plane wave model in section 2 using a standard collocation Fourier spectral method. We evaluate the quadratic non-linearities, including in the wave potential vorticity (2.6), in physical space and transform the product into Fourier space. We time march the spectral equations using an exponential time differencing method with a fourth order Runge-Kutta scheme—for details, see [Kassam & Trefethen \(2005\)](#) and [Cox & Matthews \(2002\)](#).

Our python code is available through the online repository:

<https://github.com/crocha700/niwqg>. The scripts that setup and run the simulation and the data used to produce the figures in the paper are available at: [https://github.com/crocha700/RochaWagnerYoung\\_JFM](https://github.com/crocha700/RochaWagnerYoung_JFM).

## Appendix B. Quadratic conservation laws

### B.1. Ehrenfest's theorem

To obtain (3.11) we begin by noting that with  $\mathcal{F}$  defined in (3.6)

$$\partial_t \mathcal{F} = \frac{i}{2}\lambda^2 (\phi_t \nabla \phi^* - \phi_t^* \nabla \phi) + \frac{i}{4}\lambda^2 \nabla (\phi \phi_t^* - \phi^* \phi_t). \quad (\text{B } 1)$$

Multiplying the wave equation by  $i\nabla \phi^*$ , adding to the complex conjugate, and using the expression above, one eventually finds

$$\begin{aligned} \partial_t \mathcal{F} - \frac{i}{4}\lambda^2 \nabla (\phi \phi_t^* - \phi^* \phi_t) + \frac{i}{4}\lambda^2 \eta (\Delta \phi \nabla \phi^* + \Delta \phi^* \nabla \phi) = \\ - \nabla \psi \cdot \nabla (\hat{\mathbf{k}} \times \mathcal{F}) + \eta \frac{1}{2} \zeta \nabla A + \frac{i}{2}\lambda^2 (D_\phi \nabla \phi^* - D_{\phi^*} \nabla \phi). \end{aligned} \quad (\text{B } 2)$$

Taking the domain average, and noting that the second and third terms on the left have zero average, we recover (3.11) with the dissipative term

$$\varepsilon_{\mathcal{F}} \stackrel{\text{def}}{=} \frac{i}{2}\lambda^2 \langle D_\phi \nabla \phi^* - D_{\phi^*} \nabla \phi \rangle. \quad (\text{B } 3)$$

### B.2. Wave potential energy

To obtain the wave potential energy equation (3.12) we take the dot product of  $\nabla \phi$  with gradient of the wave equation (2.8) and add the complex conjugate; the calculation is best done using index notation. The final result is

$$\begin{aligned} \mathcal{P}_t + \nabla \cdot \left[ \mathbf{u}^g \mathcal{P} + \frac{1}{2} \zeta \mathcal{F} + \frac{\lambda^2}{4} \frac{i}{2} \eta ((\nabla \phi \cdot \nabla) \nabla \phi^* - (\nabla \phi^* \cdot \nabla) \nabla \phi) \right] \\ = \frac{1}{2} \zeta \nabla \cdot \mathcal{F} - \frac{\lambda^2}{2} \phi_{,k} \sigma_{kl} \phi_{,l}^* + \frac{\lambda^2}{4} (\nabla \phi \cdot \nabla D_{\phi^*} + \nabla \phi^* \cdot \nabla D_\phi), \end{aligned} \quad (\text{B } 4)$$

where  $\mathbf{u}^g \stackrel{\text{def}}{=} \hat{\mathbf{k}} \times \nabla \psi$  is the geostrophic velocity and

$$\sigma_{kl} \stackrel{\text{def}}{=} \frac{1}{2}(u_{k,l}^g + u_{l,k}^g) \quad (\text{B5})$$

is the geostrophic strain tensor. The local equation (B4) integrates to (3.12), with the dissipative term

$$\varepsilon_{\mathcal{P}} = \frac{\lambda^2}{4} \langle \nabla \phi \cdot \nabla \mathcal{D}_{\phi^*} + \nabla \phi^* \cdot \nabla \mathcal{D}_{\phi} \rangle = -\frac{\lambda^2}{4} \langle \Delta \phi^* \mathcal{D}_{\phi} + \Delta \phi \mathcal{D}_{\phi^*} \rangle. \quad (\text{B6})$$

### B.3. Balanced kinetic energy

To obtain the balanced kinetic energy equation we first multiply the QGPV equation (2.7) by  $-\psi$ :

$$\mathcal{K}_t + \nabla \cdot [-\psi (\nabla \psi_t + \mathbf{u}^g q)] = \psi q_t^w - \psi \mathcal{D}_q. \quad (\text{B7})$$

To attack  $\psi q_t^w$  on the right, we use the expression for  $q^w$  in (3.9). Thus

$$\psi q_t^w = \nabla \cdot \underbrace{\frac{1}{2} \left[ \psi \left( \nabla \mathcal{A}_t + \frac{2}{\eta} \hat{\mathbf{k}} \times \mathcal{F}_t \right) - \nabla \psi \mathcal{A}_t \right]}_{\stackrel{\text{def}}{=} -\mathcal{H}_1} + \frac{1}{2} \zeta \mathcal{A}_t + \eta^{-1} \mathbf{u}^g \cdot \mathcal{F}_t. \quad (\text{B8})$$

Taking the dot product of (B2) with  $\mathbf{u}^g$  we have

$$\begin{aligned} \mathbf{u}^g \cdot \mathcal{F}_t = & \nabla \cdot \underbrace{\left\{ \mathbf{u}^g \left[ \frac{1}{2} \lambda^2 (\phi_{\phi^*}^* - \phi^* \phi_t) + \frac{1}{4} \eta \lambda^2 |\nabla \phi|^2 \right] - \frac{1}{4} \eta \lambda^2 [\nabla \phi \mathbf{u}^g \cdot \nabla \phi^* + \nabla \phi^* \mathbf{u}^g \cdot \nabla \phi] \right\}}_{\stackrel{\text{def}}{=} -\eta \mathcal{H}_2} \\ & + \eta \frac{1}{2} \zeta J(\psi, \mathcal{A}) + \frac{1}{2} \eta \lambda^2 \phi_{,k} \sigma_{kl} \phi_{,l}^* + \mathbf{u}^g \cdot \frac{1}{2} \lambda^2 (D_{\phi} \nabla \phi^* - D_{\phi^*} \nabla \phi). \end{aligned} \quad (\text{B9})$$

Thus

$$\partial_t \mathcal{K} + \nabla \cdot [-\psi (\nabla \psi_t + \mathbf{u}^g q) + \mathcal{H}_1 + \mathcal{H}_2] = -\zeta \nabla \cdot \mathcal{F} + \frac{1}{2} \lambda^2 \phi_{,k} \sigma_{kl} \phi_{,l}^* + \xi - \psi \mathcal{D}_q, \quad (\text{B10})$$

where

$$\xi = \frac{1}{2} f_0^{-1} (\phi^* D_{\phi} + \phi D_{\phi^*}) \frac{1}{2} \zeta + f_0^{-1} \mathbf{u}^g \cdot \frac{1}{2} (D_{\phi} \nabla \phi^* - D_{\phi^*} \nabla \phi) \quad (\text{B11})$$

is the contribution of wave dissipation to the local balanced kinetic energy budget. Interestingly, the first term on the right of (B11) reveals that the dissipation of wave action in anti-cyclones is a source of balanced kinetic energy. The second term on the right of (B11) shows that the alignment of the “action-flux dissipation vector”  $i(D_{\phi} \nabla \phi^* - D_{\phi^*} \nabla \phi)$ , with the geostrophic velocity is also a source of balanced kinetic energy. The local equation (B10) integrates to the balanced kinetic energy equation (3.13) with the dissipative terms

$$\Xi \stackrel{\text{def}}{=} \langle \xi \rangle \quad \text{and} \quad \varepsilon_{\mathcal{K}} = -\langle \psi \mathcal{D}_q \rangle. \quad (\text{B12})$$

### B.4. Specific expressions with biharmonic dissipation

The dissipative terms in (2.7) and (2.8) add small dissipation to the energy equations in section 3. The wave kinetic energy dissipation added to (3.1) is

$$\varepsilon_{\mathcal{K}} = -\nu_w \langle |\Delta \phi|^2 \rangle. \quad (\text{B13})$$

The dissipation of wave potential energy in (3.12) is

$$\varepsilon_{\mathcal{P}} = -\frac{1}{2} \lambda^2 \nu_w \langle |\nabla \Delta \phi|^2 \rangle. \quad (\text{B14})$$

Similarly, the balanced kinetic energy dissipation in (3.13) is

$$\varepsilon_{\mathcal{K}} = \kappa_e \langle \psi \Delta^2 q \rangle = \kappa_e \langle q \Delta^2 \psi \rangle. \quad (\text{B15})$$

The wave dissipation contribution to the balanced kinetic energy budget is

$$\Xi = \frac{1}{2}\nu_w f_0^{-1} \langle \frac{1}{2}\zeta (\phi^* \Delta^2 \phi + \phi \Delta^2 \phi^*) \rangle + \nu_w f_0^{-1} \langle \frac{1}{2}\psi [J(\phi^*, \Delta^2 \phi) - J(\phi, \Delta^2 \phi^*)] \rangle. \quad (\text{B } 16)$$

In all solutions of initial value problems reported in this paper, the dissipative terms (B 13), (B 14), (B 15), and (B 11) account for less—typically much less—than 10% of the energy tendencies.

## REFERENCES

- BALMFORTH, N.J., LLEWELLYN SMITH, S.G. & YOUNG, W.R. 1998 Enhanced dispersion of near-inertial waves in an idealized geostrophic flow. *Journal of Marine Research* **56** (1), 1–40.
- BALMFORTH, N.J. & YOUNG, W.R. 1999 Radiative damping of near-inertial oscillations in the mixed layer. *Journal of Marine Research* **57** (4), 561–584.
- BARKAN, R., WINTERS, K.B. & MCWILLIAMS, J.C. 2016 Stimulated imbalance and the enhancement of eddy kinetic energy dissipation by internal waves. *Journal of Physical Oceanography* **47**, 181–198.
- BRETHERTON, F.P. & GARRETT, C.J.R. 1968 Wavetrains in inhomogeneous moving media. In *Proceedings of the Royal Society of London A: Mathematical, Physical and Engineering Sciences*, , vol. 302, pp. 529–554. The Royal Society.
- BÜHLER, O. & MCINTYRE, M.E. 1998 On non-dissipative wave–mean interactions in the atmosphere or oceans. *Journal of Fluid Mechanics* **354**, 301–343.
- BÜHLER, O. & MCINTYRE, M.E. 2005 Wave capture and wave–vortex duality. *Journal of Fluid Mechanics* **534**, 67–95.
- COX, S.M. & MATTHEWS, P.C. 2002 Exponential time differencing for stiff systems. *Journal of Computational Physics* **176** (2), 430–455.
- DANIOUX, E., VANNESTE, J. & BÜHLER, O. 2015 On the concentration of near-inertial waves in anticyclones. *Journal of Fluid Mechanics* **773**, R2.
- DANIOUX, E., VANNESTE, J., KLEIN, P. & SASAKI, H. 2012 Spontaneous inertia-gravity-wave generation by surface-intensified turbulence. *Journal of Fluid Mechanics* **699**, 153–157.
- FORNBERG, B. 1977 A numerical study of 2-d turbulence. *Journal of Computational Physics* **25** (1), 1–31.
- GERTZ, A. & STRAUB, D.N. 2009 Near-inertial oscillations and the damping of midlatitude gyres: a modeling study. *Journal of Physical Oceanography* **39** (9), 2338–2350.
- KASSAM, A-K & TREFETHEN, LN 2005 Fourth-order time-stepping for stiff pdes. *SIAM Journal on Scientific Computing* **26** (4), 1214–1233.
- KLEIN, P., LLEWELLYN SMITH, S.G. & LAPEYRE, G 2004 Organization of near-inertial energy by an eddy field. *Quarterly Journal of the Royal Meteorological Society* **130** (598), 1153–1166.
- LANDAU, L.D. & LIFSHITZ, E.M. 2013 *Quantum Mechanics: Non-relativistic Theory*, , vol. 3. Elsevier.
- MCWILLIAMS, J.C. 1984 The emergence of isolated coherent vortices in turbulent flow. *Journal of Fluid Mechanics* **146**, 21–43.
- MELESHKO, V.V. & VAN HEIJST, G.J.F. 1994 On Chaplygin’s investigations of two-dimensional vortex structures in an inviscid fluid. *Journal of Fluid Mechanics* **272**, 157–182.
- MOEHLIS, J. & LLEWELLYN SMITH, S.G. 2001 Radiation of mixed layer near-inertial oscillations into the ocean interior. *Journal of Physical Oceanography* **31** (6), 1550–1560.
- NAGAI, T., TANDON, A., KUNZE, E. & MAHADEVAN, A. 2015 Spontaneous generation of near-inertial waves by the Kuroshio Front. *Journal of Physical Oceanography* **45** (9), 2381–2406.
- SALMON, R 2016 Variational treatment of inertia-gravity waves interacting with a quasigeostrophic mean flow. *Journal of Fluid Mechanics* **809**, 502–529.
- SHAKESPEARE, C.J. & HOGG, A.McC. 2017 Spontaneous surface generation and interior amplification of internal waves in a regional-scale ocean model. *Journal of Physical Oceanography* .
- TAYLOR, S. & STRAUB, D.N. 2016 Forced near-inertial motion and dissipation of low-frequency

- kinetic energy in a wind-driven channel flow. *Journal of Physical Oceanography* **46** (1), 79–93.
- THOMAS, L. N. 2012 On the effects of frontogenetic strain on symmetric instability and inertigravity waves. *Journal of Fluid Mechanics* **711**, 620640.
- VANNESTE, J. 2013 Balance and spontaneous wave generation in geophysical flows. *Annual Reviews of Fluid Mechanics* .
- WAGNER, G.L. & YOUNG, W.R. 2015 Available potential vorticity and wave-averaged quasi-geostrophic flow. *Journal of Fluid Mechanics* **785**, 401–424.
- WAGNER, G.L. & YOUNG, W.R. 2016 A three-component model for the coupled evolution of near-inertial waves, quasi-geostrophic flow and the near-inertial second harmonic. *Journal of Fluid Mechanics* **802**, 806–837.
- XIE, J.-H. & VANNESTE, J. 2015 A generalised-lagrangian-mean model of the interactions between near-inertial waves and mean flow. *Journal of Fluid Mechanics* **774**, 143–169.
- YOUNG, W.R. & BEN JELLOUL, M. 1997 Propagation of near-inertial oscillations through a geostrophic flow. *Journal of Marine Research* **55** (4), 735–766.
- YOUNG, W.R., RHINES, P.B. & GARRETT, C.J.R. 1982 Shear-flow dispersion, internal waves and horizontal mixing in the ocean. *Journal of Physical Oceanography* **12** (6), 515–527.